Research Square

Preprints are preliminary reports that have not undergone peer review.
They should not be considered conclusive, used to inform clinical practice,
or referenced by the media as validated information.

A material selective capture model predicts cargo specific RNA granule retention at active synapses

Ayberk Alp Gyunesh

ayberkalp.gyunesh@stud.unibas.ch

University of Basel

Article

Keywords:

Posted Date: November 5th, 2026

DOI: https://doi.org/10.21203/rs.3.rs-11412438/v1

License: This work is licensed under a Creative Commons Attribution 4.0 International License.
Read Full License

Additional Declarations: No competing interests reported.

A material-selective capture model predicts cargo-specific RNA-granule retention at active synapses

Ayberk Alp Gyunesh[1]

[1]*University of Basel, Basel, Switzerland*

* Correspondence: ayberkalp.gyunesh@stud.unibas.ch

Abstract

Synapses maintain distinct functional states despite continual molecular turnover, yet how a synapse selects the RNA–protein granules that renew it from shared dendritic traffic is unclear. Here it is shown that any docking rule blind to cargo identity preserves the composition of the encountered granule pool, so selective capture requires an identity-bearing variable. Material compatibility between granule and postsynaptic density condensate is proposed as this variable and formalized in a stochastic model separating encounter, docking, productive capture and feedback. Disrupting cargo-to-material correspondence abolishes selective enrichment, whereas removing material selectivity increases off-target capture. In three mouse and rat subcellular transcriptome datasets, localized transcripts have higher 3′UTR guanine and GC content than matched somatic transcripts; coupling this variation to published postsynaptic material measurements shifts modelled capture towards localized cargo, and shuffling the assignment removes the shift. Material compatibility is a testable selection rule through which synaptic identity may persist by selective renewal.

Introduction

Many forms of long-lasting synaptic plasticity depend on local protein synthesis and must persist despite the continual turnover of synaptic proteins [1,2]. Because neighbouring synapses share much of the same dendritic transport and biosynthetic environment, maintaining a plastic change requires mechanisms that restrict reinforcement to selected synaptic sites [3,4]. Single-spine stimulation increases nascent protein supply across a local synaptic neighbourhood even though structural enlargement remains concentrated at the stimulated spine, indicating that spatially restricted protein production and synapse-specific functional reinforcement are not equivalent [5]. Synaptic tagging and capture provides a conceptual solution by proposing that recent activity establishes a transient local tag enabling an activated synapse to capture plasticity-related products, but activity determines where and when capture is permitted rather than which molecular cargo should be selected [4,6]. Neighbouring synapses share a heterogeneous pool of mobile messenger ribonucleoproteins (mRNPs), an activated synapse may encounter several candidate granules, while the same granule may pass multiple potential capture sites [7–9]. The unresolved specificity problem is therefore how an eligible synapse preferentially retains an appropriate mRNP and converts that encounter into productive local cargo use [4,9,10]. Neurons transport diverse mRNAs into dendrites as dynamic mRNP particles whose localization and translational competence are shaped by cis-regulatory RNA elements and trans-acting factors such as RNA-binding proteins (RBPs) [3,7,11,12]. Alternative 3′UTR isoforms can differ in their somatic or neuropil enrichment, stability, and translational regulation, indicating that transcripts encoding the same protein need not share the same subcellular fate [11]. Live-particle imaging has shown bidirectional transport, pauses, and transcript-dependent docking at synapses, and the Rgs4 3′UTR mediates activity-dependent recruitment through Staufen2 [9,11,13]. Local glutamate uncaging similarly recruits β-actin mRNA to stimulated spines, where local translation contributes to spine stabilization [10]. Importantly, plasticity-induced enrichment of an mRNA near a spine can be uncoupled from its translational state [10,14], and spine entry of TDP-43/FMRP-bound Rac1 mRNA leads to translational activation or repression depending on the mGluR activation state [15]. These observations motivate a mechanistic distinction between a granule reaching the synaptic neighbourhood, undergoing persistent docking, and producing a local functional consequence [9,11]. The synaptic sushi-belt model proposes that mobile mRNPs patrol multiple synaptic sites and are captured in response to

local demand rather than delivered to a predetermined address, and its mathematical formalization showed that trafficking and detachment rules alone face morphology-dependent trade-offs without specifying how an eligible synapse selects among molecularly heterogeneous granules already present in its local encounter pool [8,16]. Synaptic tagging and consolidation models correspondingly explain how activity establishes eligibility and how slower dynamics stabilize synaptic change [4,17,18]. Several molecularly distinct mRNPs are locally available [8,9,14]. Given this local availability, why does one granule persistently dock and become productive while another does not? The here described Material-selective capture (MSC) hypothesis proposes that this missing post-encounter selection rule could arise from material compatibility between an RNA–protein granule and the local postsynaptic density *(*PSD) condensate. RNA is not merely passive cargo: sequence, secondary structure, intermolecular RNA–RNA interactions, and RBP composition can alter condensate assembly, internal dynamics, and emergent material properties [19–21]. Increasing RNA guanine content, for example, reduced molecular dynamics and increased the viscosity of FMRP-containing condensates, although stable G-quadruplex formation was not itself sufficient to explain the full material shift [22]. The postsynaptic density is likewise organized through multivalent scaffold interactions that generate compositionally selective condensates [23,24], and native and reconstituted PSD condensates exhibit soft-glass-like behaviour governed by percolation of the scaffold network [25]. Disrupting Shank3 SAM-domain oligomerization softened the PSD condensate, increased molecular mobility, and impaired synaptic transmission and plasticity [25]. Because both compartments can occupy composition-dependent material states, MSC predicts that the relevant variable for synaptic retention is not the state of either compartment alone but their relative material mismatch. Here, MSC is formalized as a stochastic mechanistic model in which granule transport and synaptic encounter are separated from physical docking and productive capture, so that spatial availability, persistent retention, and downstream reinforcement can be analysed as distinct stages [9,10,14]. Within this hierarchy, the activity tag determines when a synapse is capture-permissive, material mismatch biases which encountered granules dock and become productive, and delayed productive payload reinforces a consolidation state that in turn strengthens a slower material-memory tag. This work compares full MSC with five prespecified control variants that disrupt material selectivity, cargo-to-material correspondence, dimensionality, or feedback, and authentic mismatch is additionally separated from model-used mismatch to test whether simulated docking follows the supplied material representation rather than

an undeclared cargo label. The model predicts that organized cargo-to-material correspondence improves productive-capture enrichment and limits crosstalk beyond activity-dependent capture alone, whereas material-memory feedback stabilizes local capture competence and generates protocol-dependent history dependence. By coupling sequence-derived transcript variation to experimentally anchored PSD material states, MSC further predicts that changes in PSD material properties shift relative docking preferences among transcript-associated granules [4,11,22,25–27]. These predictions are falsifiable through independent measurement of RNP and PSD material features, 3′UTR and RBP perturbations, and encounter-conditioned single-particle tracking combined with local translation reporters [9,10].

Results

Material compatibility extends activity-dependent synaptic tagging

Neuronal activity can transiently mark synapses as eligible for plasticity, but an activity tag alone does not specify which RNA–protein granules should be retained from a heterogeneous dendritic pool. Therefore, the MSC model was developed within this framework to test whether compatibility between granule and postsynaptic material states could provide an additional post-encounter layer of selectivity. In this framework, dendritic transport determines which granules become spatially available, the activity tag T_i determines when a synapse becomes capture-permissive, and pair-specific material mismatch biases which encountered granules undergo physical docking and productive capture (***Fig. 1A-D***). Each granule g was assigned an effective material-state vector $\mathbf{u}_g$, and each synapse i was assigned a target material-state vector θi. Operationally, material identity denotes the effective material-state vector assigned to a granule or synapse in the model. Organized material identity denotes the correspondence between authentic cargo identity and the material-state representation supplied to the docking mechanism. For each granule–synapse pair, compatibility was quantified by the normalized squared material mismatch d_{ig}^2, with lower values indicating greater compatibility. Material mismatch is therefore a relational quantity defined between two material states, rather than an intrinsic score assigned to either the granule or the synapse alone. The model

implemented an encounter–docking–productive capture hierarchy through a six-step stochastic update cycle (***Fig. 1***). First, a spatial encounter gate identified granule–synapse pairs within the capture radius. The docking hazard for each encountered pair was then jointly determined by T_i, the material-memory tag M_i, and d_{ig}^2, and physical docking was sampled as a Bernoulli event. Docked events became productive only when their compatibility-weighted effective payload exceeded the productivity threshold. Productive events delivered delayed reinforcement to the consolidation state S_i, which subsequently reinforced M_i and thereby increased future docking competence (***Fig. 1D***). Thus, MSC separates spatial availability, persistent retention, productive cargo use, and feedback-dependent stabilization as distinct computational stages. Docking probability decreased monotonically with increasing material mismatch (***Fig. 2A***). Stratification of encounter opportunities by synapse state showed that this mismatch-dependent relationship was retained within both active and inactive synapses, whereas the elevated lowest-mismatch bin in the pooled analysis reflected enrichment of active-synapse encounters (***Fig. S1***). A logistic observation model fitted to simulated encounter opportunities recovered the encoded effect directions: T_i and M_i positively predicted physical docking, whereas d_{ig}^2 negatively predicted docking (***Fig. 2B***). Physical docking constituted the principal bottleneck in the event hierarchy: approximately 0.3% of encounter opportunities produced a docking event, whereas approximately 67% of docked events became productive (***Fig. 2C***). Because an encounter opportunity denotes one eligible granule–synapse pair-step rather than one unique physical visit, these percentages quantify event-level transitions in the simulation. The model therefore predicts that selectivity is imposed primarily during encounter-to-docking conversion, with an additional compatibility-dependent filter operating after docking.

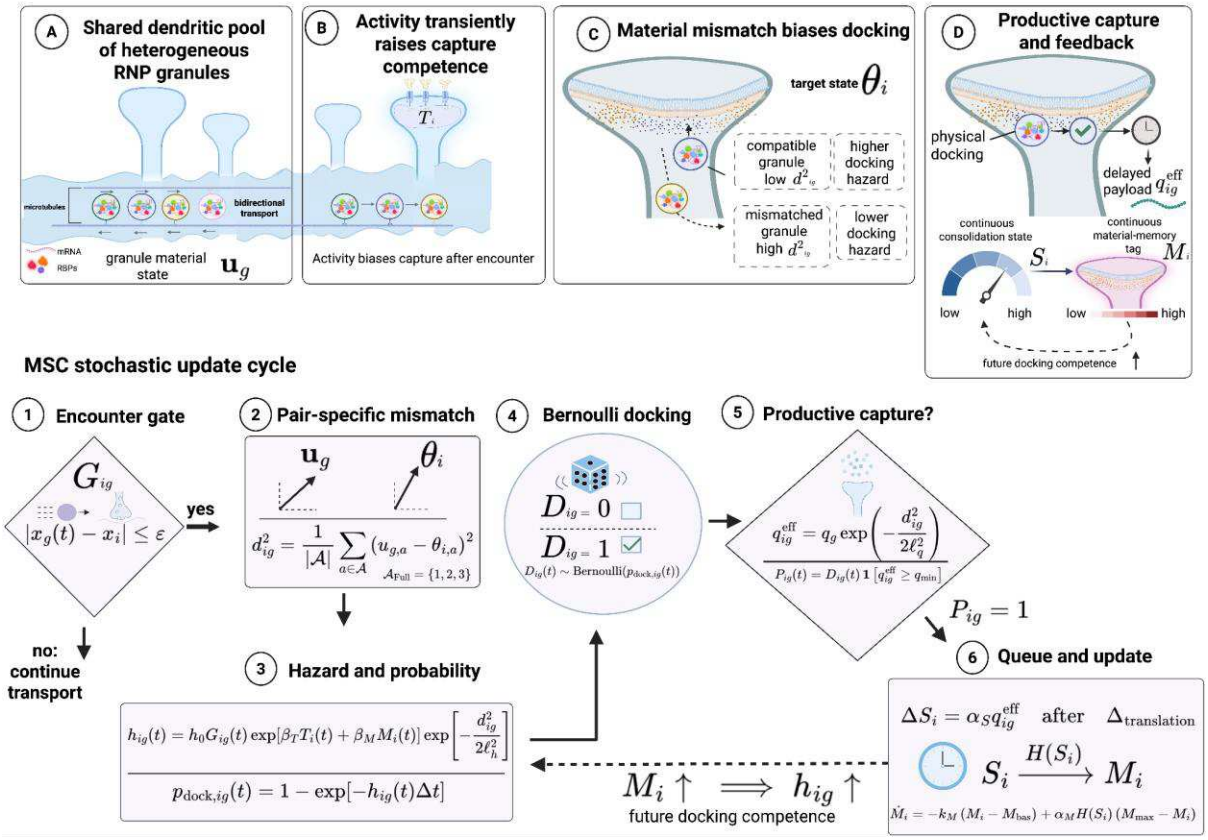


Figure 1. Conceptual framework and stochastic update cycle of the MSC model.
(A) Heterogeneous RNA–protein granules undergo bidirectional transport within a shared dendritic pool. Each granule g carries an effective material-state vector u_g, a coarse-grained description of composition-dependent RNP properties. **(B)** Synaptic activity transiently raises local capture competence through the activity tag T_i, which determines when synapse i becomes capture-permissive after a spatial encounter. **(C)** Material compatibility determines which encountered granules preferentially dock. Each synapse carries a target material state θicompatibility for the pair is quantified by the normalized material mismatch d_{ig}; lower mismatch increases the docking hazard, whereas higher mismatch suppresses it. **(D)** A docked granule becomes productive only when its compatibility-weighted effective payload exceeds the productivity threshold $q_{\min}$. Productive events enter a delayed reinforcement queue and subsequently reinforce the consolidation state S_i, which reinforces the slower material-memory tag M_i and thereby increases future docking competence. The lower schematic summarizes the resulting stochastic update cycle, in which encounter, mismatch evaluation, hazard-based docking, the productivity gate and delayed feedback are applied once per simulation step.

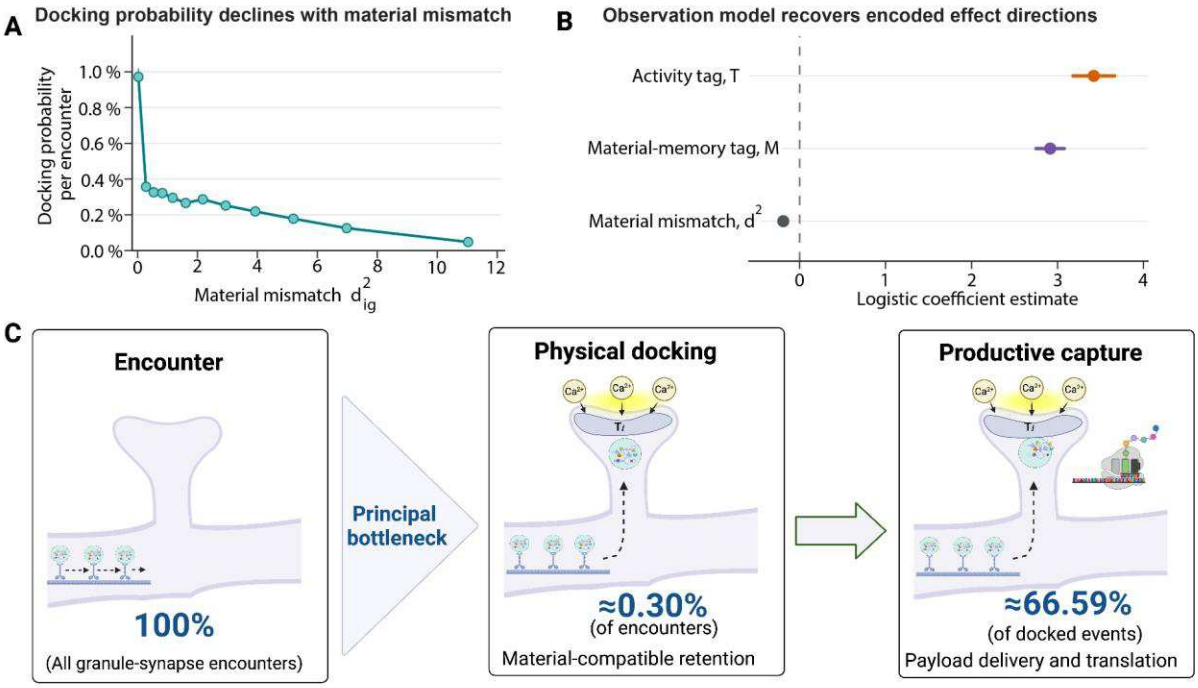


Figure 2. Mechanistic validation of the MSC docking model.

(A) Docking probability per encounter opportunity across 12 quantile bins of the model-used squared material mismatch d_{ig}, which decreases monotonically with increasing mismatch. **(B)** Coefficients of the logistic observation model fitted to 2,000,000 encounter observations from 400 parameter seeds: the activity tag and the material-memory tag promote docking, whereas material mismatch suppresses it. Points show coefficient estimates and horizontal bars model-based 95% confidence intervals. **(C)** The encounter–docking–productive-capture hierarchy. Physical docking is the principal bottleneck: approximately 0.3% of encounter opportunities produce a docking event, of which approximately 67% become productive.

Organized material identity and feedback support distinct components of synaptic specificity

To determine whether the specificity generated by the full MSC model depended on organized material identity, feedback, or both, the model was compared with capture-only, projected-1D, shuffled-material, random-material, and activity-only variants across 400 matched stochastic seeds (***Fig. 3A–D; Supplementary Note 1***). The full MSC model generated preferential consolidation at active synapses, whereas disrupting the correspondence between granule and synaptic material states reduced this specificity (***Fig. 3A***). The strongest reductions occurred in the shuffled-material and random-material variants, indicating that disrupting the correspondence between authentic cargo identity and the model-used material representation reduced consolidation specificity. Feedback made a distinct contribution to the material-memory state. The full MSC model established material-memory specificity at active synapses, whereas the capture-only variant, despite retaining material-dependent

docking, did not generate persistent material-memory specificity (***Fig. 3B***). Thus, the model separates the initial selection of compatible granules from the subsequent stabilization of local capture competence. Organized material identity also supported productive-capture enrichment. In the full MSC model, productively captured granules were enriched relative to their availability in the shared pool, whereas shuffled-material and random-material controls fell below the no-enrichment reference (***Fig. 3C***). This loss of enrichment indicates that preserving the distribution of material values is insufficient when their correspondence to granule identity is disrupted. Paired per-seed comparisons showed that material-disrupting controls produced the largest deficits across consolidation specificity, material-memory specificity, productive-capture enrichment, and strong docking (***Fig. 3D***). By contrast, the projected-1D and activity-only variants retained some aggregate outcomes, showing that these readouts alone do not establish material-selective capture. In particular, activity-only feedback generated consolidation specificity of comparable magnitude to Full MSC, but produced greater off-target crosstalk, especially for the material-memory state (***Fig. 3A; Fig S5.***). Together, these simulations predict that material compatibility primarily determines capture quality, whereas feedback converts selective capture into a persistent local material-memory state. More generally, an identity-blind docking rule cannot enrich any cargo class beyond its representation in the locally encountered pool, irrespective of synaptic activity or cargo-independent feedback (***Supplementary Note 2***). Cargo-selective docking therefore requires an identity-bearing variable, which MSC implements through pair-specific material mismatch. We next tested whether this mechanistic separation remained detectable when granule material identity varied over time. Across the numerically resolved and equilibrated regime, weak-to-moderate fluctuations preserved consolidation specificity close to static MSC, whereas the largest fluctuation amplitude reduced specificity by approximately 10% when the material-relaxation and encounter timescales were comparable ***(Fig. S2 A,C ; Supplementary Note 3)***. Docking-stage strong-granule enrichment remained close to its static value, whereas material-memory specificity and downstream consolidation were more sensitive to drift and more sensitive to material fluctuations ***(Fig. S2 A,B)***. The model therefore predicts that time-varying material identity primarily disrupts the temporal coherence required to reinforce persistent material memory rather than abolishing instantaneous compatibility filtering.

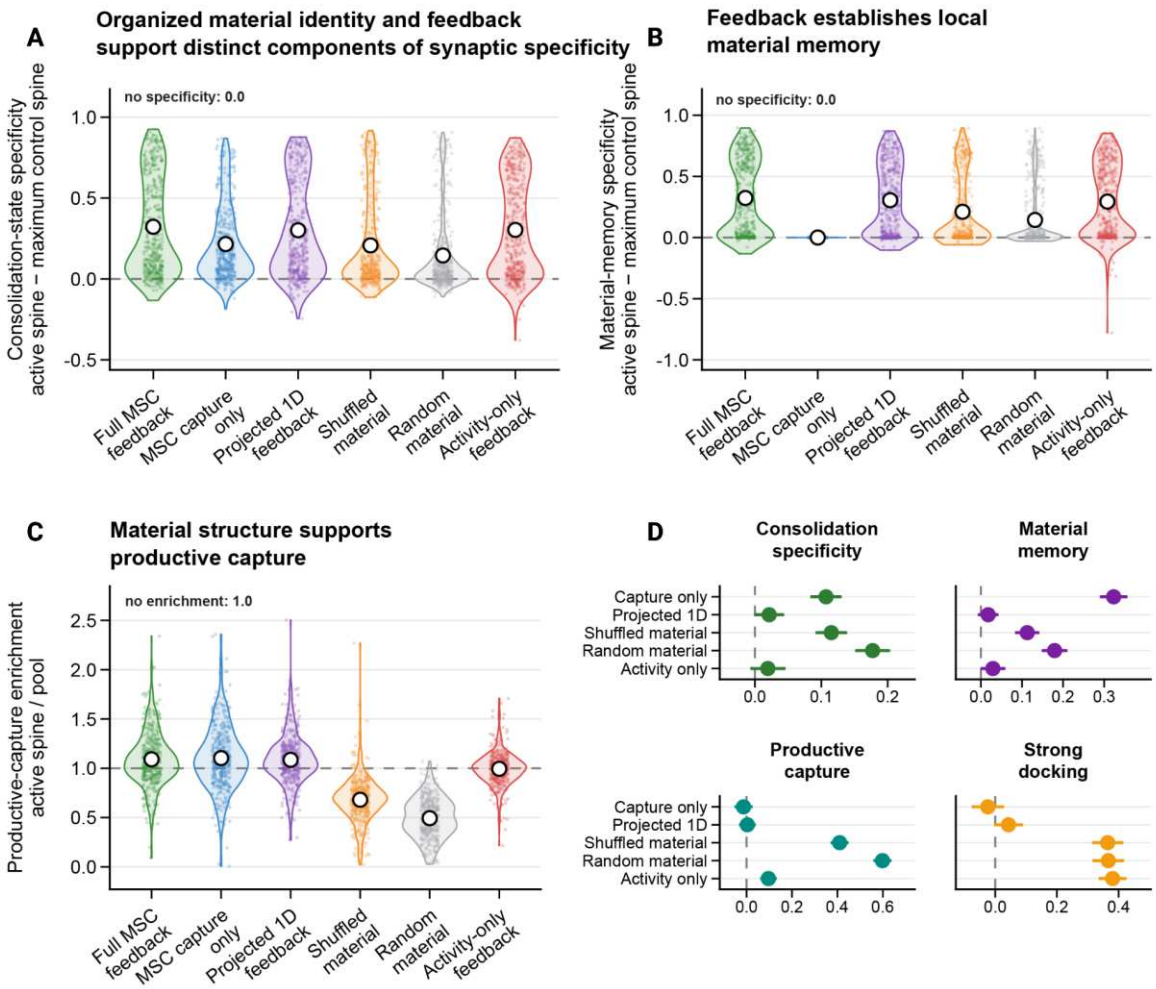


Figure 3. Organized material identity and feedback support distinct components of synaptic specificity.

Per-seed simulations compare the full Material-Selective Capture (MSC) feedback model with capture-only, projected-1D, shuffled-material, random-material and activity-only controls (n = 400 matched parameter seeds per model). **(A)** Full MSC generates active-synapse consolidation specificity, which is reduced most strongly when material identity is shuffled or randomized. **(B)** Feedback establishes a local material-memory state, whereas capture without feedback produces no material-memory specificity. **(C)** Organized material identity supports productive capture: full MSC is enriched above the available granule pool, whereas shuffled- and random-material controls fall below the no-enrichment reference. **(D)** Paired within-seed differences between full MSC and each control show that material disruption produces the largest deficits in consolidation specificity, material memory, productive capture and strong-granule docking, whereas projected-1D and activity-only controls retain several aggregate outcomes. Violin plots show per-seed distributions with white circles indicating means, dashed lines denote no specificity or no enrichment, and forest-plot intervals show approximate 95% confidence intervals.

Slow material feedback generates history-dependent synaptic memory

It was next tested whether feedback between productive capture, consolidation, and the material-memory state generated history-dependent synaptic responses. A stateful stepped-drive protocol was applied in which the activity drive was increased from 0 to 1 and subsequently decreased to 0, while the complete simulation state was propagated continuously between successive drive plateaus (***Fig. 4A; see Methods***). The drive represents a graded activity or firing-rate proxy rather than action-potential amplitude. The late consolidation state S followed distinct trajectories during the increasing and decreasing branches of the stateful stepped-drive protocol (***Fig. 4B***). At matched drive levels, S was generally higher during the decreasing branch after prior exposure to stronger activation. The maximum mean branch separation occurred after return to zero drive and reached $\Delta S = 0.43$. The material-memory state M showed a similar history-dependent response, with a maximum mean branch separation of $\Delta M = 0.48$ at zero drive (***Fig. 4C***). Thus, both states depended not only on the current activation drive but also on the preceding activation history. Branch separation was positive across most of the drive range and approached zero at high drive, where both states saturated (***Fig. 4D***). To summarize history dependence across the full drive range, the signed area between the decreasing and increasing branches was calculated separately for each parameter seed using trapezoidal integration. Signed hysteresis areas were positive for both S and M across 100 parameter seeds (one-sided Wilcoxon signed-rank tests: S, $W = 5048$, $p = 2.07 \times 10^{-18}$; M, $W = 5036$, $p = 2.97 \times 10^{-18}$; ***Fig. 4E***). Together, these results show that the full MSC feedback model generates protocol-dependent history dependence without requiring an explicitly imposed discrete state switch. Targeted variation of the Hill coefficient further showed that increasing feedback cooperativity strengthened integrated branch separation while modestly reducing late-state specificity under the transient-pulse protocol (***Fig. S3 E,F***).

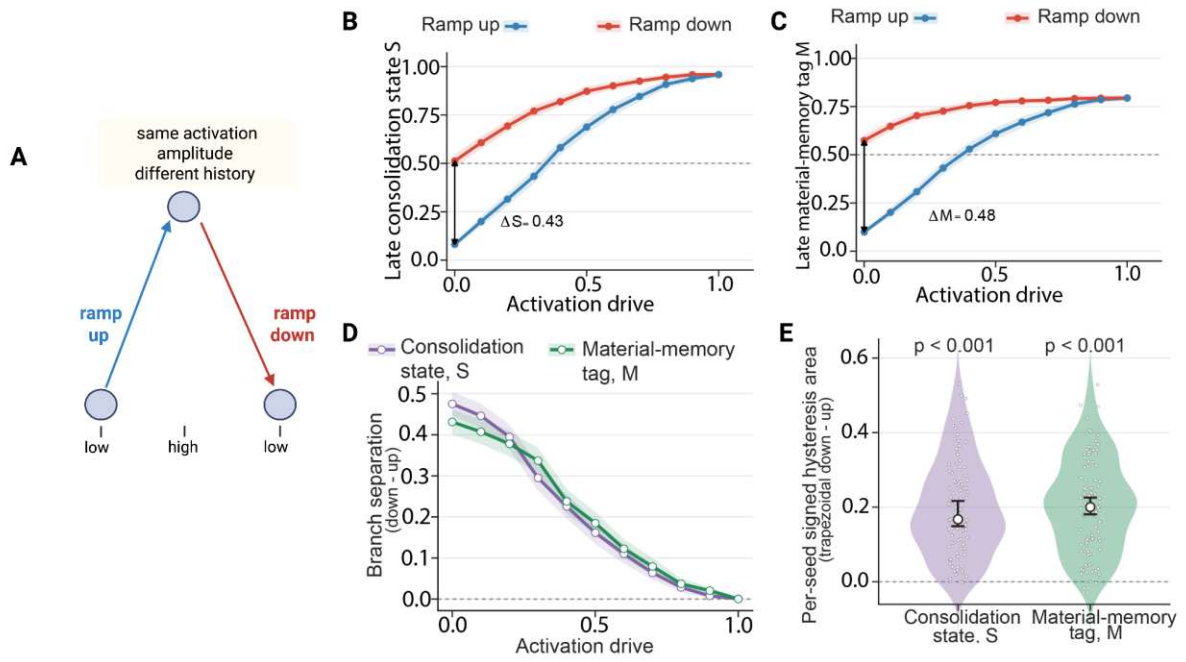


Figure 4. Slow material feedback generates protocol-dependent history dependence in the MSC model.

(A) Stateful stepped-drive protocol: the activity drive of the active synapse was increased from 0 to 1.0 and decreased back to 0 in increments of 0.1, each of the eleven plateaus per branch lasting 4,200 s, with the complete simulation state propagated continuously between plateaus. **(B)** Late consolidation state S during the increasing and decreasing branches; the decreasing branch remains elevated after prior exposure to higher drive, with a maximum mean branch separation of ΔS at zero drive. **(C)** Late material-memory state M under the same protocol, with a maximum mean branch separation of ΔM at zero drive. **(D)** Drive-resolved branch separation, defined as decreasing minus increasing values for S and M; the dashed line denotes zero separation. **(E)** Per-seed signed hysteresis areas obtained by trapezoidal integration of branch separation across the matched drive levels. Points show individual parameter seeds, violins the seed-level distributions, white circles medians and black intervals bootstrap 95% confidence intervals for the median; both distributions exceeded zero by one-sided Wilcoxon signed-rank tests. Late states were averaged over the final 600 s of each plateau and summarized across 100 parameter seeds; lines and shading in (**B–D**) show mean and SEM.

Docking follows model-used material mismatch rather than authentic cargo identity

It was next tested whether the association between material mismatch and docking arose specifically from the material representation supplied to the model. For each granule synapse pair, the true material mismatch was distinguished d^2_{true}, calculated from the authentic cargo identity, from the model-used material mismatch d^2_{used}, calculated from the representation supplied to the docking rule (***Fig. 5A***). The construction of authentic and model-used material representations and the corresponding control logic are detailed in ***Supplementary Notes 1 and 4***. Without this separation, apparent material selectivity could merely reflect how cargo classes were initially labelled rather than

285 the mismatch evaluated by the docking rule. First the association between d^2_{true} and docking was
286 estimated while adjusting for the activity tag T and, where estimable, the material-memory tag M
287 (***Fig. 5B***). True material mismatch negatively predicted docking in variants that preserved the
288 authentic material mapping. By contrast, its estimated effect approached zero when this mapping was
289 randomized or removed, and the random-material and activity-only coefficients fell within the
290 prespecified negligible-effect interval of ± 0.03 logit units under Holm-adjusted equivalence tests.
291 Then, d^2_{true} and d^2_{used} were entered as separate predictors (***Fig. 5C***). Their coefficients overlapped in
292 material-preserving variants because both variables encoded the same granule synapse
293 correspondence. After material shuffling or randomization, however, d^2_{used} retained a negative
294 association with docking, whereas the independent association of d^2_{true} approached zero. This
295 separation shows that the docking mechanism tracked the material mismatch provided to the model
296 rather than authentic cargo identity itself. These analyses found no evidence of an additional cargo-
297 identity effect on docking after disruption of the cargo-to-material correspondence. Additionally, the
298 true-mismatch coefficients were translated into odds ratios for an increase from the 25th to the 75th
299 percentile of d^2_{true} (***Fig. 5D***). Odds ratios below one indicated reduced docking odds with increasing
300 authentic mismatch, whereas values approaching one indicated little or no remaining association.
301 These analyses used 100 stochastic seeds and 1,000,000 sampled encounters per model variant.
302 Together, the anti-tautology analysis predicts that docking is governed by d^2_{used}, not by unobserved
303 access to d^2_{true}. Authentic material identity predicts docking only when it remains aligned with the
304 material representation supplied to the MSC docking mechanism.

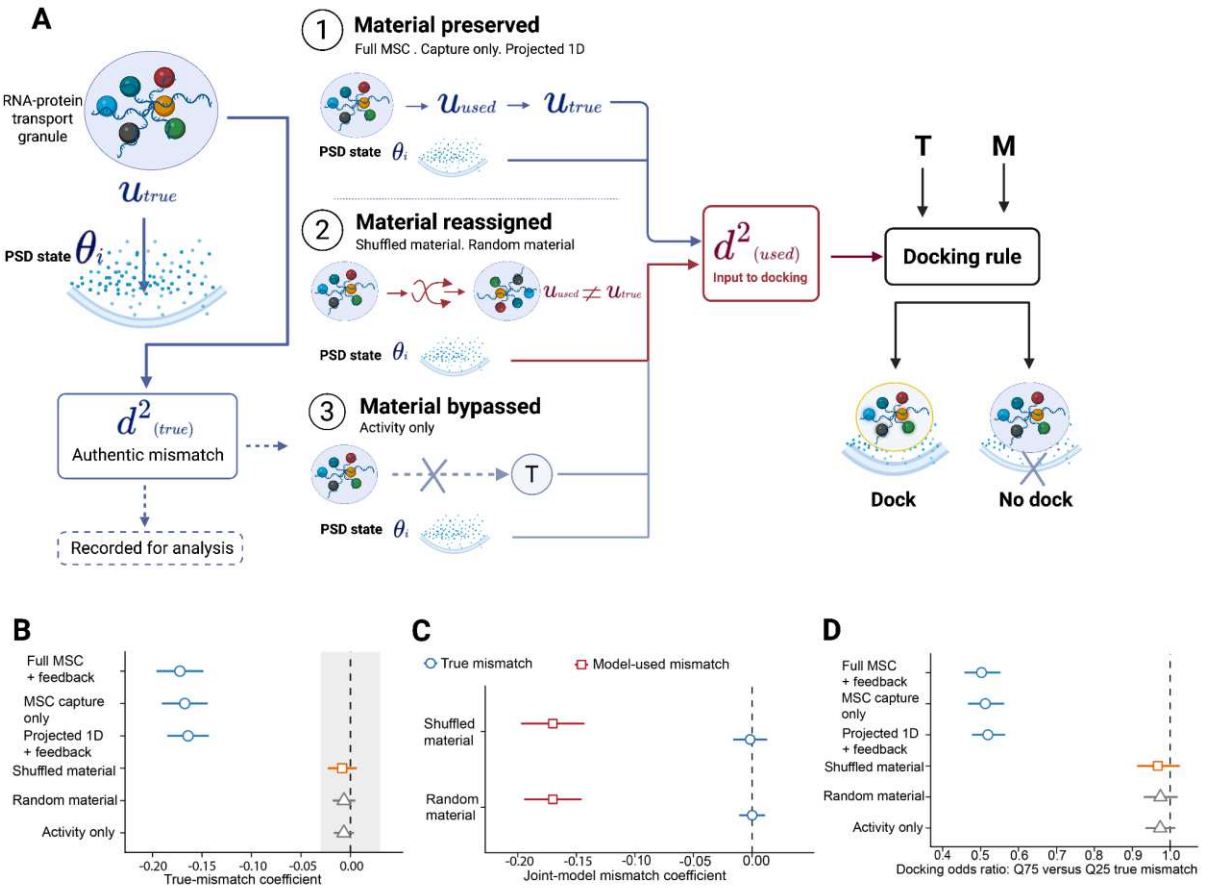


Figure 5. Docking tracks model-used material mismatch without latent access to authentic cargo identity.

(A) Schematic of the anti-tautology design: true material mismatch was calculated from authentic cargo identity, whereas model-used mismatch was calculated from the representation supplied to each variant's docking rule. The two quantities are identical in material-preserving variants and separate after material shuffling or randomization. **(B)** Seed-fixed-effect logistic coefficients relating true mismatch to docking, adjusted for the activity tag and, where estimable, the material-memory tag. The shaded region denotes the prespecified negligible-effect interval of ±0.03 logit units; random-material and activity-only coefficients were equivalent to zero by Holm-adjusted two one-sided tests. **(C)** True- and model-used-mismatch coefficients entered separately. The two overlap in material-preserving variants, whereas after shuffling or randomization authentic mismatch approaches zero and model-used mismatch retains a strong negative association with docking; joint models indicated that only model-used mismatch independently predicted docking in these variants. **(D)** Odds ratios for an increase from the 25th to the 75th percentile of true mismatch, where values below one indicate reduced docking odds at greater mismatch. Models used seed-clustered standard errors; points show estimates and bars 95% confidence intervals. Results derive from 100 simulation seeds and 1,000,000 sampled encounter opportunities per variant.

Sequence-derived transcript variation couples to PSD material state to bias active capture preference

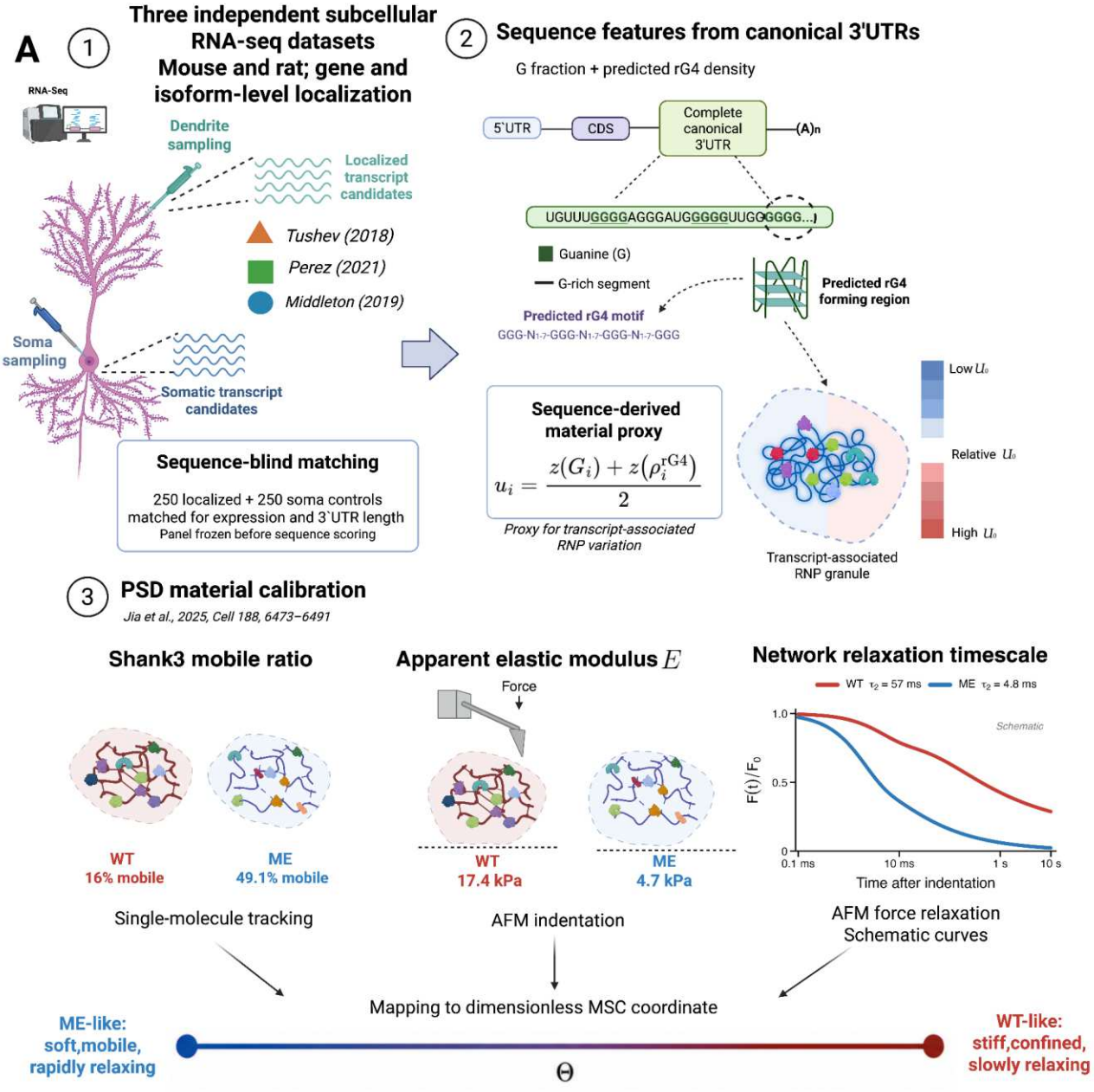
The next question was whether transcript-associated sequence variation could be coupled to experimentally anchored PSD material states within the MSC framework. To address this, a data-to-model workflow was constructed that combined three independent subcellular RNA-seq resources, 3′UTR sequence features, and published measurements of PSD material properties (***Fig. 6A***). The transcriptomic resources comprised a mouse gene-level soma–dendrite dataset from *Middleton et al.*, a rat gene-level dataset from *Perez et al.*, and a rat isoform-resolved CA1 soma–neuropil dataset from *Tushev et al.* [11,26,27]. These datasets therefore span two species, gene- and isoform-level analysis, and distinct experimental definitions of localized RNA. For each resource, we constructed a frozen, sequence-blind panel containing 250 localized transcripts or isoforms and 250 somatic controls matched for expression and 3′UTR length. Transcript selection and matching were completed before calculation of any sequence-derived feature. Sequence features were extracted from annotation-prioritized representative 3′UTRs for the gene-level datasets and from experimentally defined PASS 3′UTR isoforms for the Tushev dataset. For transcript or isoform i, the primary sequence-derived transcript coordinate was defined as

$$u_i = \frac{z(G_i) + z\left(\rho_i^{\mathrm{rG4}}\right)}{2}$$

where G_i is the 3′UTR G fraction and ρ_i^{rG4} is the predicted density of merged rG4-forming regions per kilobase. Both features were standardized within the corresponding frozen transcript panel. This coordinate was used as a proxy for transcript-associated RNP variation and not as a direct measurement of granule viscosity, stiffness, relaxation dynamics, or phase state. The primary G+rG4 coordinate was elevated in localized relative to matched somatic transcript populations in all three datasets, with paired mean differences of approximately 0.32 z units in Middleton, 0.47 in Perez, and 0.55 in Tushev (***Fig. 6B***). G content alone showed an even larger and consistently positive difference across the three resources. Raw predicted rG4 density was most clearly elevated in the isoform-resolved Tushev dataset, whereas its effect was weaker and less precisely resolved in the two gene-level datasets. After adjustment for G fraction and log 3′UTR length, residual rG4 density was centred near zero across datasets. GC content was also strongly elevated, while the 3′UTR-length control remained close to zero following matching. Shuffled and random score controls likewise showed no

reproducible localized–somatic difference (***Fig. S4C ; Supplementary Note 5***). These results therefore identify reproducible G/GC-associated 3′UTR variation in localized transcripts, rather than establishing an independent or causal effect of predicted rG4 density on RNA localization. Next, three experimentally measured PSD observables were mapped, used here as kinetic proxies for contact relaxation (***see Discussion***), onto separate dimensionless PSD coordinates , Θ, oriented from an ME-like state—softer, more mobile, and more rapidly relaxing—to a WT-like state—stiffer, more confined, and more slowly relaxing (***Fig. 6A)***. Network relaxation time, apparent elastic modulus, and Shank3 mobile fraction were mapped independently using published WT and oligomerization-deficient Shank3 measurements [25]. A phenomenological cross-scale gain of 0.55 produced oriented WT-like and ME-like coordinate anchors of approximately ± 0.83, ± 0.44, and ± 0.38 for relaxation time, elastic modulus, and mobile fraction, respectively. These independent mappings test whether the predicted direction depends on a particular PSD observable; their effect magnitudes should not be compared quantitatively because the coordinate separations differ by construction. Across all three PSD mappings, the MSC model predicted positive WT-like minus ME-like shifts in relative localized-cargo preference for the primary G+rG4 and G-content coordinates (***Fig. 6D***). At the relaxation-time mapping and the productive-capture stage, the shift for the primary coordinate was 0.023 (95% CI 0.010–0.037; $q = 6.0 \times 10^{-3}$) in Middleton, 0.043 (0.029–0.059; $q = 4.0 \times 10^{-4}$) in Perez, and 0.053 (0.039–0.068; $q = 2.3 \times 10^{-4}$) in Tushev. Positive shifts indicate that the WT-like PSD state increased the modelled relative preference for localized over matched somatic transcript-associated granules. The predicted direction was reproduced across the Middleton, Perez, and Tushev resources and was generally more pronounced after the productive-capture gate than at the physical-docking stage. This pattern is consistent with the narrower compatibility filter applied during productive capture. The absolute preferences underlying these differences are shown for the relaxation-time mapping at productive capture in ***Fig. 6C***: in Tushev, localized preference moved from 0.457 in the ME-like state to 0.509 in the WT-like state for the primary coordinate and from 0.436 to 0.534 for G content, whereas the shuffled-mapping control remained at 0.487 in both states. The corresponding absolute preferences for all three mappings and both outcome stages are shown in ***Fig. S4 A,B .*** To test whether the predicted shifts depended on organized transcript-to-coordinate correspondence, the assignment of sequence-derived coordinates was shuffled among transcript identities while preserving the marginal distribution of coordinate values. Shuffling reduced or abolished the WT-like

minus ME-like shift (***Fig. 6D***). Direct primary-minus-shuffled contrasts at the relaxation-time mapping were positive in all three resources and reached significance in the two datasets with finer localization resolution: 0.034 ($q = 9.0 \times 10^{-4}$) in Perez and 0.052 ($q = 2.3 \times 10^{-4}$) in Tushev at productive capture, whereas the Middleton contrast was positive but not significant ($q = 0.30$) (***Fig. 6E***). Thus, the prediction depended on the correspondence between transcript identity and the model-used sequence coordinate rather than on the score distribution alone. The same qualitative direction was retained when relative preference was expressed as a log localized-to-somatic capture-rate ratio rather than as a bounded preference fraction (***Fig. S4D ; Supplementary Note 5***). Because the cross-scale mapping is phenomenological, the mean WT-ME coordinate separation was additionally varied from zero to twice its reference value. Authentic mappings produced predominantly positive WT-like shifts across non-zero scalings, whereas shuffled mappings were generally smaller and more variable. Thus, the predicted direction was not restricted to the reference scaling, although its magnitude remained scaling dependent (***Fig. S4E ; Supplementary Note 5***). This analysis validates the internal dependency of the sequence-anchored MSC instantiation: the model responds to the transcript-associated coordinate supplied to its capture rule, and the predicted state-dependent shift weakens when that correspondence is disrupted. It does not independently establish that the sequence-derived coordinate is a biological measurement of RNP material identity or that G-rich sequence acts through condensate material properties in vivo. Together, the results support the experimentally testable prediction that transcript-associated 3′UTR variation can interact with PSD material state to bias relative physical docking and productive-capture preference. The broader qualitative MSC prediction also remained robust to two additional sources of material variability. Because neuronal mRNAs are frequently transported as single- or low-copy RNPs, granules containing N transcript copies were tested with N = 10 serving as an upper stress condition. Copy number, implemented as a reduction in within-class material variance proportional to $1/\sqrt{N}$, produced little systematic change in strong-granule enrichment or consolidation specificity (***Fig. S2D,E; Supplementary Note 3***). Activity-dependent movement of the synaptic target vector likewise produced only a moderate reduction at the highest drift rate tested (***Fig. S2***). MSC therefore does not require granule or PSD material coordinates to remain perfectly static, although sufficiently large or rapid changes reduce the temporal consistency of selective reinforcement.


A
1
Three independent subcellular RNA-seq datasets
Mouse and rat; gene and isoform-level localization
RNA-Seq
Dendrite sampling
Localized transcript candidates
Tushev (2018)
Perez (2021)
Middleton (2019)
Soma sampling
Somatic transcript candidates
Sequence-blind matching
250 localized + 250 soma controls matched for expression and 3`UTR length
Panel frozen before sequence scoring
2
Sequence features from canonical 3'UTRs
G fraction + predicted rG4 density
5`UTR
CDS
Complete canonical 3'UTR
(A)n
UGUUUGGGGAGGGAUGGGGUUGGGGGG...)
Guanine (G)
G-rich segment
Predicted rG4 motif
GGG-N1-7-GGG-N1-7-GGG-N1-7-GGG
Predicted rG4 forming region
Sequence-derived material proxy
$u_i = \frac{z(G_i) + z(\rho_i^{rG4})}{2}$
Proxy for transcript-associated RNP variation
Low U_0
Relative U_0
High U_0
Transcript-associated RNP granule
3
PSD material calibration
Jia et al., 2025, Cell 188, 6473–6491
Shank3 mobile ratio
WT
16% mobile
ME
49.1% mobile
Single-molecule tracking
Apparent elastic modulus E
Force
WT
17.4 kPa
ME
4.7 kPa
AFM indentation
Network relaxation timescale
WT τ_2 = 57 ms
ME τ_2 = 4.8 ms
Schematic
F(t)/F0
1.0
0.5
0
0.1 ms
10 ms
1 s
10 s
Time after indentation
AFM force relaxation
Schematic curves
Mapping to dimensionless MSC coordinate
ME-like:
soft,mobile,
rapidly relaxing
WT-like:
stiff,confined,
slowly relaxing
Θ

409

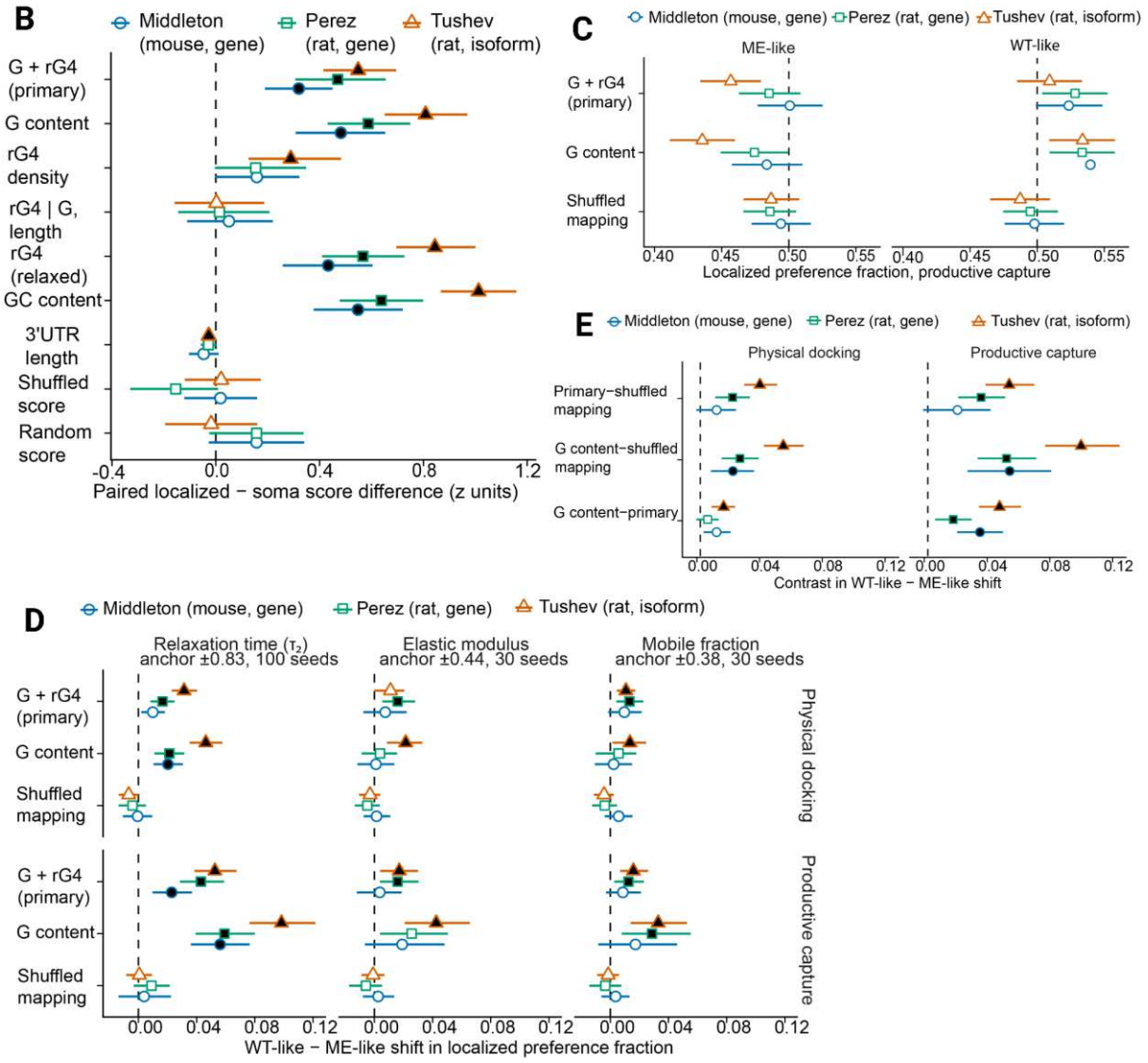


Figure 6. Sequence-derived transcript variation couples to PSD material state to bias active capture preference.

(A) Data-to-model workflow integrating three subcellular RNA-seq resources — Middleton (mouse, gene level), Perez (rat, gene level) and Tushev (rat, 3′UTR-isoform level) — with published PSD material measurements. For each dataset, 250 localized transcripts or isoforms were matched to 250 somatic controls by expression and 3′UTR length before any sequence scoring, and PSD relaxation time, elastic modulus and Shank3 mobile fraction were mapped independently onto an ME-like-to-WT-like coordinate. **(B)** Paired sequence-score differences between localized and matched somatic transcripts for the primary G+rG4 coordinate, its components and the prespecified controls; positive values indicate higher scores among localized transcripts. **(C)** Absolute relative preference for localized cargo in the ME-like and WT-like PSD states, for the relaxation-time mapping at productive capture; the dashed line at 0.5 denotes no preference. **(D)** WT-like minus ME-like shifts in relative localized-cargo preference for physical docking and productive capture across all three PSD mappings; the shuffled-mapping control preserves the coordinate values while disrupting their assignment to transcript identities. **(E)** Primary-minus-shuffled contrasts at the relaxation-time mapping, showing that the state-dependent preference depends on organized transcript-to-coordinate correspondence rather than on the coordinate

distribution alone. Colours denote Middleton (blue circles), Perez (green squares) and Tushev (orange triangles). Error bars show 95% confidence intervals from 20,000 bootstrap resamples across 250 matched pairs in (B) and from seed bootstraps across 100 matched seeds for relaxation time and 30 seeds each for elastic modulus and mobile fraction in (C–E); filled symbols indicate $q < 0.05$ after Benjamini–Hochberg correction.

Discussion

The MSC hypothesis addresses a specificity problem that activity-dependent synaptic tagging alone cannot resolve. Synaptic tagging and capture proposes that activity marks a synapse as eligible to receive plasticity-related products, but an activity tag does not specify which RNA–protein granule should be retained from a heterogeneous dendritic pool [4,6]. MSC adds a second layer: the activity tag determines when capture is permitted, whereas material mismatch influences which encountered granules dock and become productively used. The strongest constraint on this problem is independent of any parameter choice. Conditional on the granules that encounter a synapse, any docking rule that does not use cargo identity preserves the cargo composition of the encountered pool in distribution, so that activity and cargo-independent feedback change how much is captured but not what is captured (***Supplementary Note 2***). Cargo-selective capture therefore requires an identity-bearing variable in the capture step. Two qualifications follow. The result is pointwise in synapse, time, and pre-event history, so aggregation across synapses can produce apparent compositional differences that reflect cargo availability rather than docking-stage selection. Here, material mismatch is one possible implementation rather than the only one, since motor or adaptor identity, sequence-specific recognition by RNA-binding proteins, RNA–RNA interactions or RNA modifications could equally break exchangeability [8,12,19,28]. MSC is therefore best read as one concrete, testable instance of a general requirement. The encounter–docking–productive-capture hierarchy predicts that spatial opportunity, persistent retention, and productive cargo use are distinct levels of organization, and each has an experimental analogue: local glutamate uncaging recruits β-actin mRNA to stimulated spines and induces its local translation [10], the Rgs4 3′UTR controls transport bias and activity-dependent docking or undocking [9,10], and TDP-43/FMRP-associated Rac1 mRNA can enter spines without detectable translational reactivation under prolonged group-I mGluR stimulation [15]. The control variants assessed here show that consolidation and cargo selection are related but non-equivalent outcomes. Activity-only MSC retained activity-dependent capture and feedback but lacked a granule-specific material filter, whereas the shuffled- and random-material controls retained formally material-

dependent rules while breaking the link between authentic cargo identity and the material representation supplied to them; their loss of productive-capture enrichment shows that preserving the distribution of material values is insufficient once those values no longer carry organized information about cargo identity (***Fig. 3***). A mechanism can therefore elevate a postsynaptic consolidation state without solving the stricter problem of selecting appropriate cargo. Consistent with this, only model-used mismatch retained an independent association with docking after shuffling, while the effect of authentic mismatch approached zero (***Fig. 5***), which validates the internal causal implementation of the model but does not establish that equivalent material coordinates exist biologically. Within this architecture, mismatch and feedback perform different functions: mismatch determines relative capture quality, whereas consolidation-to-material-memory feedback stabilizes local capture competence after productive events. Consolidation and material memory followed distinct increasing and decreasing branches under the stateful stepped-drive protocol (***Fig. 4***). This hysteresis is dynamic and protocol dependent; it does not demonstrate equilibrium bistability or identify a molecular switch, and greater feedback cooperativity strengthened branch separation while modestly reducing late-state specificity under transient stimulation (***Fig. S3***). Global sensitivity analysis identifies a bounded regime in which encounter supply, activity-dependent docking and productive reinforcement predominantly determine whether consolidation develops, whereas material-space parameters control captured-cargo composition (***Fig. S3***). Bounded material fluctuations are tolerated, whereas changes on the encounter timescale weaken persistent reinforcement (***Fig. S2***). MSC treats material identity as an effective consequence of RNA sequence and structure, RBP composition, multivalency and molecular mobility [20,22], consistent with evidence that neuronal RNA localization depends on combinations of cis-regulatory elements and trans-acting RBPs [9,11,12]. Alternative 3′UTRs alter localization, stability and translational control, and the nervous system preferentially expresses extended isoforms carrying additional RBP- and microRNA-binding sites and structural elements [11,29,30]; truncation of the long Bdnf 3′UTR impaired dendritic localization, spine maturation and dendritic LTP despite largely preserved total BDNF [31]. MSC suggests a testable extension: by expanding the available sequence and structural interaction space, long neuronal 3′UTRs could help specify distinct RBP compositions and RNP material states rather than merely carrying individual localization elements. Shortening a 3′UTR would then reduce material-state separability even when the coding sequence is unchanged, and systematic shortening, extension or exchange of selected

3′UTRs should alter docking conditional on encounter and increase crosstalk between cargo populations. This remains speculative, because the established effects of long 3′UTRs concern localization, stability and translation [11,12] rather than condensate-level material identity; a decisive experiment would compare matched short and long isoforms while independently measuring abundance, dendritic transport, RBP composition, particle mobility, spine-proximal dwell time and local translation, since behavioural changes alone would not distinguish material-selective capture from established effects of 3′UTR perturbation. Clinically, 3′UTR variation is already implicated in neuronal dysfunction, including a FMR1 variant that eliminates activity-dependent local translation without changing the coding sequence [30,32], and loss of dendritic CaMKIIα mRNA reduces postsynaptic CaMKIIα, late-phase LTP and memory consolidation [33]; MSC offers the complementary interpretation that altered 3′UTRs change not only transport or abundance but also the material representation available for compatibility-dependent docking. RNA modifications could add a further layer, since m6A-dependent changes in RNA structure and reader binding can promote or inhibit assembly of functionally distinct protein–RNA complexes on an otherwise unchanged transcript [28,34]; the present model contains no explicit modification variable, and a future extension would predict that modification changes affect capture only when they also change independently measured material properties. The postsynaptic side of MSC is motivated by the condensate organization of the PSD, in which multivalent interactions among PSD-95, SynGAP, GKAP/SAPAP, Shank and Homer generate condensed assemblies whose composition and dynamics respond to molecular perturbation [23,24]. Activity also reorganizes this architecture over longer timescales: after chemical LTP, rapid spine enlargement preceded slower increases in PSD-95 assembly size and nanoscale complexity, consistent with treating the postsynaptic target as a slowly evolving state rather than a fixed structure, although nanoarchitecture is not itself a material measurement [35]. Jia et al. further showed that native and reconstituted PSD condensates exhibit soft-glass-like properties governed by percolation of the scaffold network, and that disrupting Shank3 SAM-domain oligomerization softened the condensate, increased molecular mobility, impaired synaptic transmission and LTP, and produced social and social-memory phenotypes [25]. MSC suggests one possible downstream consequence: beyond altering receptor anchoring directly, a shift in PSD material properties could change compatibility with particular RNP granules and therefore the composition of locally retained RNA, linking PSD material state, local protein renewal and synaptic dysfunction. More broadly, MSC raises the possibility that

synaptic identity is maintained not by indefinitely stable molecular components but by material-dependent selection rules that recursively guide their local renewal. These experiments do not demonstrate defective RNA-granule capture, and MSC should not be presented as an established explanation of the reported behavioural phenotypes [25]. The narrower falsifiable prediction is that Shank3 material-state perturbations produce cargo-dependent changes in RNP dwell time and local translation rather than a uniform reduction in recruitment of all RNAs, and that restoring the PSD material state restores the capture profile even if total PSD protein abundance is not fully normalized. If capture selectivity depends on RNP–PSD material compatibility, two intervention classes become conceptually distinct: cargo-side approaches would modify the transcript rather than the protein product, for example by redirecting alternative polyadenylation with antisense oligonucleotides [36,37] or by delivering engineered transcripts with defined 3′UTRs, whereas postsynaptic approaches would target the receiving compartment, consistent with evidence that Shank3 oligomerization sets PSD material properties [25] and that adult restoration of Shank3 expression rescues a subset of autism-related phenotypes in mice [38]. MSC predicts that these strategies are not interchangeable, since correcting only one side may fail if the mismatch between compartments is not restored, although no therapeutic prediction of MSC has yet been tested. A multi-synapse extension could finally test whether synapses of the same engram acquire partially convergent target material states, which is not evaluated here. The current model remains a coarse-grained *in silico* framework. Granule and PSD material vectors are effective coordinates rather than measurements, equal weighting of the material axes is an operational assumption, and the compatible and incompatible granule populations impose controlled heterogeneity without representing discrete biological RNP classes. The most direct route to replacing them is interfacial. Both compartments are condensates, so whether an encountered granule is retained is in principle a three-phase wetting problem set by the granule/cytoplasm, PSD/cytoplasm and granule–PSD interfacial tensions, as relative interfacial tensions govern the architecture of other multiphase condensates [39,40]. In that reading the relevant observables are these tensions and the viscoelastic dissipation at the contact rather than any single bulk property, and material mismatch is a phenomenological stand-in for the corresponding interfacial cost. The distinction matters because bulk rheology and molecular-scale dynamics are not interchangeable descriptions of a condensate's material state: dense phases can be orders of magnitude more viscous than water while their constituent chains reconfigure on sub-microsecond timescales [41]. In multiphase

condensates, interfacial tensions set the equilibrium architecture, whereas the viscosity-to-surface-tension ratio sets the timescale of coalescence and shape relaxation [40]. Because RNP–PSD encounters are transient, docking in MSC is a kinetic rather than an equilibrium outcome; bulk viscoelastic observables can therefore constrain how rapidly a contact relaxes into persistent association, even though they do not determine equilibrium adhesion. The PSD observables in ***Fig 6*** are used in this kinetic sense, and equilibrium adhesion would additionally require interfacial measurements. Which observable the compatibility rule should ultimately depend on remains open, and no interfacial measurement currently exists for RNP–PSD pairs. The one-dimensional geometry omits spine morphology, dendritic branching, cytoskeletal organization, local crowding and competition among overlapping capture zones; simulated docking is an event-level transition rather than an explicit bound trajectory, and productive capture coarse-grains granule remodelling, RNA accessibility, translation initiation and incorporation into postsynaptic structures. The sequence-derived coordinate in ***Fig 6*** combines 3′UTR G content and predicted rG4 density and is therefore a proxy rather than a measured RNP material state, and the PSD coordinate maps heterogeneous observables onto a common dimensionless axis through a phenomenological cross-scale gain, so that agreement among independently oriented PSD observables supports the direction of the prediction without calibrating distances between biological material states; consistent with this, the predicted direction was retained across a broad range of PSD-coordinate scalings while its magnitude remained scaling dependent (***Fig. S4***). The central experimental requirement is therefore to measure material-associated properties independently of capture, to separate encounter frequency from persistent docking by single-particle tracking, and to add a local translation reporter that distinguishes docking from productive capture (***Supplementary Note 6***). Because these tests depend on fluorescent reporters, labelling itself is a potential confound: fluorescent-protein and peptide tags can enhance, suppress or abolish condensation and alter recruitment and condensate dynamics in a tag- and protein-specific manner [42], and even sparse tagged spike-ins can perturb condensate number in vivo and misreport exchange dynamics [43]. Material-associated measurements on either side of the RNP–PSD interface should therefore be validated across multiple tags and near-endogenous expression levels, and compared with untagged or minimally labelled references where possible. MSC would be supported if independently measured material mismatch predicts docking beyond activity, cargo abundance, transport dynamics and encounter frequency, and if orthogonal

manipulation of the PSD state produces cargo-dependent rather than uniform changes in docking; it would be weakened if material-changing perturbations affect only encounter frequency, if PSD perturbations alter all cargo classes uniformly, or if activity, abundance and transport fully explain docking once material measurements are included. Wet-lab validation is required before MSC can be assigned a causal role in synaptic RNA capture, memory consolidation or neurodevelopmental disease.

Methods

Model scope and architecture

MSC is a coarse-grained stochastic model of granule transport, synaptic encounter, physical docking, productive capture and delayed postsynaptic reinforcement, and it does not resolve individual molecular binding reactions, condensate thermodynamics, translation-initiation steps or protein incorporation. As in earlier quantitative treatments of dendritic mRNA trafficking, localization and synaptic capture, transport and retention are represented as effective processes rather than molecular reactions [8,16,44]. Mobile granules and heterogeneous synapses occupy a shared one-dimensional domain: granule g carries an effective material vector u_g, synapse i carries a target material vector θi, and their compatibility is the normalized material mismatch d_{ig}, while each synapse additionally carries a transient activity tag T_i, a slower material-memory tag M_i and a consolidation state S_i. Conditional on spatial encounter, T_i, M_i and d_{ig} determine a stochastic docking hazard; docked granules pass a stricter compatibility-dependent productivity gate; and productive capture delivers payload after a translation delay, reinforcing S_i and, through nonlinear feedback, M_i. Complete event definitions, update ordering and the computational implementation are provided in ***Supplementary Notes 4, 7-9***.

Material-state representation

Each granule and synapse was assigned a D-dimensional vector representing a coarse-grained material fingerprint, motivated by evidence that condensates occupy composition-dependent viscoelastic states and that RNA and protein sequence features tune their viscosity, elasticity and relaxation dynamics [20,22,45,46] and that condensate material states evolve over time through dynamic arrest and aging modulated by RNA and ATP-dependent activity [21]. Compatibility between granule g and synapse i was quantified as the normalized material mismatch d_{ig} (***Fig. 1***; ***Supplementary Note 4***), where lower values denote greater compatibility and all material coordinates entered with equal weight. The same scalar mismatch enters the docking and productive-capture stages through stage-specific compatibility kernels. Material-space construction, coordinate scaling, variant-specific mappings and the distinction between authentic and model-used material vectors are specified in ***Supplementary Note 4.***

Spatial encounter gate

Granule–synapse proximity was represented by a binary encounter gate that equals one when granule g lies within the encounter half-width ε of synapse i and zero otherwise; because the gate multiplies the docking hazard, the hazard vanishes outside this region. The gate therefore defines spatial eligibility only, separating spatial opportunity from activity- and material-dependent selection. The scale of ε is motivated by the reported mass, dimensions and molecular organization of the PSD [47,48] rather than equated with a PSD radius, and ε remained small relative to the modelled inter-site spacing. Transport, boundary conditions, encounter detection and repeated-contact handling are specified in ***Supplementary Notes 7 and 8***

Stochastic docking

Conditional on spatial encounter, physical docking was modelled as a stochastic event governed by the continuous-time hazard (***Fig. 1; Supplementary Note 8***), in which the baseline hazard h_0 is modulated multiplicatively by the encounter gate, exponentially by the activity tag T and the material-memory tag M with coefficients β_T and β_M, and by a Gaussian material-compatibility kernel of width ℓ_h acting on the mismatch d_{ig}. Activity and material memory therefore increase docking competence, whereas increasing mismatch suppresses it. Assuming the hazard remained constant within one simulation step, it was converted into the finite-step docking probability (***Fig. 1; Supplementary Note***

8) and the binary docking event was sampled as a Bernoulli draw, so that docking is a stochastic output of the mechanism rather than an additional model input. The Gaussian term provides a graded compatibility filter and is not a microscopic thermodynamic derivation. Sampled parameter values and admissible ranges are reported in ***Supplementary Table S1***; hazard conversion, repeated-contact handling, simultaneous-candidate constraints and the operational interpretation of simulated docking are specified in ***Supplementary Note 8.***.

Productive capture and delayed payload delivery

Physical docking did not necessarily result in productive cargo use. For each docked pair we calculated a compatibility-weighted effective payload from the intrinsic productive capacity of the granule and a second Gaussian kernel of width ℓ_q acting on the model-used mismatch, and classified the event as productive when this payload reached the productivity threshold $q_{\min}$ (***Fig. 1;*** ***Supplementary Note 9***). Because ℓ_q was defined as a sampled fraction of the docking width, $\ell_q < \ell_h$ productive capture imposed a stricter compatibility requirement than physical docking. Intrinsic productive capacity was assigned from the authentic granule vector relative to the active-synapse target and fixed when the granule pool was generated, so that cargo quality remained independent of any subsequent reassignment of the material representation used by the capture kernels (***Supplementary Note 4***). Productive events entered a pending-input queue and delivered their payload after the translation delay $\delta_{\mathrm{translation}}$, sampled between 300 and 900 s, which coarse-grains granule remodelling, transcript accessibility, translation initiation and the action of the translated product on a timescale consistent with activity-induced local RNA accumulation and translation [10,14] and with delayed plasticity-related product supply in tagging models [49]. Both $q_{\min}$ and the productive-capture transition are operational model assumptions rather than molecularly derived discontinuities.

Synaptic state dynamics

Each synapse carries three bounded state variables representing distinct temporal layers: the transient activity tag T, the consolidation state S and the slower material-memory tag M. The activity tag followed a leaky integrator with decay timescale τ_T, sampled between 900 and 3,600 s in agreement with the transient and reversible lifetime of synaptic tags [4,6], and received a single increment of amplitude A at the activation time; it entered the docking hazard but did not determine

whether a docked event became productive. The consolidation state decayed with timescale τ_S and received an increment $\alpha_S q_{\mathrm{eff}}$ for every productive event after the translation delay, so that S integrated the timing, frequency and effective payload of recent productive capture, whereas nonproductive docking contributed nothing. Material memory relaxed toward a basal level M_{bas} at rate k_M and was reinforced as a Hill function of S with half-activation K_M, cooperativity n_H and upper bound $M_{\max}$ (***Fig. 1D; Supplementary Note 9***), closing the feedback loop because M enters the docking hazard with coefficient β_M. The Hill term produces graded, threshold-like reinforcement without imposing a discrete state switch, so MSC does not require the biochemical bistability postulated by several models of late-LTP maintenance [49]. Feedback increased general docking competence but carried no cargo information, so material compatibility remained necessary for selectivity. All states were clipped to the unit interval and should be read as effective variables rather than concentrations of identified molecules; initial conditions, sampled ranges and the discrete update order are given in ***Supplementary Tables S1 and S2 and Supplementary Note 9.***

Model variants and controls

To separate the contributions of material-dependent capture, material dimensionality, cargo-to-material correspondence and consolidation-dependent feedback, six prespecified variants were evaluated: full MSC; capture-only, in which consolidation-dependent reinforcement of M was disabled; projected-1D, in which mismatch was recalculated from the first material coordinate; shuffled-material, in which model-used vectors were permuted across granule identities; random-material, in which model-used vectors were drawn independently of authentic identity; and activity-only, in which the material-compatibility factors were removed from both capture rules (***Fig 3; Supplementary Note 1***). Unless explicitly modified, all variants retained the same transport process, encounter definition, activity-tag dynamics, intrinsic productive-capacity framework, delayed-payload framework, simulation duration, parameter draws and outcome definitions, and corresponding variants were evaluated using matched parameter-generating seeds. Authentic and model-used material representations were stored separately in every variant, which enabled calculation of true and model-used mismatch for the anti-tautology analysis (***Fig 5; Supplementary Note 4***). Projected-1D is a dimensionality control rather than evidence that biological material states are intrinsically one-dimensional, since projection changes the geometry and scale of pairwise distances. The activity-only

variant is identity-blind at the docking stage, so that conditional on encounter and synaptic state all cargo classes share the same docking probability; ***Supplementary Note 2*** proves analytically that such a rule preserves the cargo composition of the encountered pool in distribution and therefore cannot generate systematic docking-stage cargo enrichment. Complete definitions of the retained and disrupted components, material mappings and variant-specific transition rules are provided in ***Supplementary Note 1.***

Simulation design and parameter sampling

Baseline simulations were performed for 3,600 s using a fixed timestep of $\Delta t = 2$. The one-dimensional domain had length L sampled between 80 and 180 model-distance units and contained 18–35 evenly spaced synapses, and the number of mobile granules was derived from domain length and granule density, $N_{\mathrm{gran}} = \mathrm{round}(L\rho_g)$, with $\rho_g$between 0.60 and 1.30 granules per model-distance unit. Granules were initialized at uniformly distributed positions and moved by a persistent drift–diffusion process with reflecting boundaries; transport speed, diffusion coefficient, direction-switching probability and capture radius were sampled independently for each parameter realization, with intervals motivated by microtubule-dependent, bidirectional and saltatory transport of RNA-containing granules in dendrites [13,50]. Unless otherwise indicated, the central synapse was designated active and received a single activity-tag increment of amplitude 1.0 at the activation time, all synaptic states were initialized at their basal values, and the delayed-payload queue was empty. The material space contained four coordinates, of which the first three entered the primary full-MSC mismatch while the fourth, outcome-associated coordinate was excluded to reduce circularity; the projected-1D variant used only the first coordinate. Synaptic target vectors were sampled from a standard normal distribution, after which the target of the active synapse was set to the origin. Continuous parameters were sampled independently from the uniform intervals in ***Supplementary Table S1***, the number of synapses and the Hill coefficient from discrete uniform distributions, whereas the number of granules and the productive-capture kernel width were derived rather than sampled independently. For the primary comparison, each parameter-generating seed defined one parameter realization shared across all six variants, while deterministic variant-specific seeds governed initialization, transport and stochastic event sampling; the design therefore matched parameter realizations across variants without imposing identical random-event histories, and variant effects were evaluated by pairing

716 outcomes within the shared parameter-generating seed. Fixed and derived quantities, initialization
717 rules and simulation settings are provided in ***Supplementary Tables S1 and S2***.

718 **Global sensitivity analysis**

719 Global sensitivity was evaluated across 500 Latin-hypercube parameter sets spanning the 27
720 sampling intervals in ***Supplementary Table S1***, generated from a fixed design seed, with integer
721 parameters mapped to their admissible range. Each parameter set was evaluated using four
722 independent stochastic replicates whose outcomes were averaged before analysis. Partial rank
723 correlation coefficients were calculated on rank-transformed parameters and outcomes after
724 regressing out the remaining 26 parameters, and Spearman correlations were retained as unadjusted
725 complements; p-values were corrected within each of the six reported outcomes using the Benjamini–
726 Hochberg procedure [51]. Targeted one-parameter profiles varied twelve mechanistically central
727 parameters across seven values each, linearly spaced except for h_0, k_M and α_M, which were spaced
728 logarithmically, while all remaining parameters were held at the midpoint of their intervals; each value
729 was evaluated with 30 stochastic replicates. Hill-dependent hysteresis profiles used 15 replicates for
730 each $n_H \in \{3, 4, 5, 6\}$. Full definitions and results are provided in ***Supplementary Note 3 and Fig.***
731 ***S3***.

732 **Outcome definitions and summary metrics**

733 Late-state readouts were calculated as the arithmetic mean of each state variable over the final 600 s
734 of the corresponding simulation or plateau. Consolidation specificity was defined as the late
735 consolidation state of the active synapse minus the maximum late consolidation state among all
736 inactive synapses, and material-memory specificity analogously; comparison with the strongest
737 inactive synapse is a conservative measure that prevents weak average activity across many inactive
738 synapses from inflating the apparent active-synapse advantage. An encounter opportunity was
739 defined as one granule–synapse pair located within the capture radius during one simulation step, so
740 that a granule remaining within the radius for several steps contributes several opportunities,
741 consistent with repeated evaluation of the finite-step docking probability. The conditional docking
742 probability was the number of sampled docking events divided by the number of eligible pair-steps,
743 and the conditional productive fraction was the number of productive events divided by the number of

docking events. These denominators were kept distinct because spatial eligibility, physical docking and productive capture are nested but mechanistically different stages, and both quantities should be interpreted as transition probabilities per eligible simulation opportunity rather than per unique granule–synapse contact episode. Material enrichment among active-synapse docking events was expressed relative to the composition of the available granule pool, with productive-payload enrichment defined analogously, so that a value of one indicates no preferential capture and values above or below one indicate enrichment or depletion. All outcome metrics were calculated separately for each parameter-generating seed before aggregation across seeds.

Stateful stepped-drive history-dependence protocol

The activity drive of the active synapse was increased from 0 to 1.0 and subsequently decreased to 0 in increments of 0.1, giving eleven plateaus per branch, and the drive was treated as a dimensionless graded activity or firing-rate proxy rather than an action-potential amplitude. Each plateau lasted 4,200 s, during which the activity tag of the active synapse was clamped at the corresponding drive level while all remaining variables evolved according to the MSC dynamics. The complete simulation state was propagated continuously between successive plateaus without reinitialization, including the consolidation state, the material-memory tag, granule positions and transport directions, granule material vectors, synaptic target vectors, the random-number-generator state and the pending-payload queue, so that the decreasing branch retained the state accumulated during the increasing branch. The drive level 1.0 occurred once at the end of the increasing branch and once at the beginning of the decreasing branch, and these consecutive plateaus were deliberately retained as separate branch-specific observations. For each parameter seed, branch direction and drive level, the active-synapse state was averaged over the final 600 s, and branch separation was defined as the decreasing minus the increasing value at matched drive levels, with positive values indicating persistence after earlier exposure to stronger activation. The primary seed-level measure of history dependence was the signed hysteresis area, obtained by trapezoidal integration of branch separation across the eleven matched drive levels and tested against zero across 100 independently sampled parameter seeds using one-sided Wilcoxon signed-rank tests with the prespecified directional alternative.

Statistical analyses and model comparisons

Parameter-generating seeds were the independent units for simulation-level outcomes, whereas granule–synapse encounter opportunities were the observational units in event-level docking models; encounters, docking events, synapses and time points sampled within one simulation were not treated as independent simulation replicates. To verify that simulated docking reflected the encoded MSC mechanism, a logistic observation model containing the activity tag, the material-memory tag, material mismatch and an active-synapse indicator was fitted to 2,000,000 encounter observations drawn from 400 parameter seeds, which contained 6,079 physical-docking events; the expected coefficient directions were positive for the activity and material-memory tags and negative for material mismatch (***Fig 2B***). This observation model was used as a diagnostic summary of simulated events rather than as an independently fitted mechanistic model. Variant comparisons used 400 parameter-generating seeds per variant, and differences between full MSC and each control were calculated within matched parameter-generating seeds before aggregation (***Fig 3***). For the anti-tautology analysis, seed-fixed-effect logistic models with seed-clustered standard errors were fitted to 100 simulation seeds and 1,000,000 sampled encounter opportunities per variant; true and model-used mismatch were stored and analysed separately and jointly, equivalence to a negligible effect was evaluated by two one-sided tests against a prespecified interval of ±0.03 logit units [52], and the resulting p-values were adjusted across the tested variants using the Holm procedure [53]. True-mismatch coefficients were additionally converted into odds ratios for an increase from the 25th to the 75th percentile of true mismatch (***Fig 5***). Multiple comparisons across the prespecified sequence coordinates, outcomes and PSD mappings were controlled using the Benjamini–Hochberg procedure and are reported as q values [54]. All statistical tests were two-sided unless a directional hypothesis was specified in advance, as for the positive hysteresis-area tests, and interpretation emphasized effect direction, magnitude and uncertainty rather than p-values alone.

Transcriptomic datasets and panel construction

Transcript-associated 3'UTR variation was evaluated using three independent subcellular transcriptomic datasets: the mouse soma–dendrite dataset of Middleton et al. (GEO GSE115480), the rat soma–dendrite dataset of Perez et al. (GEO GSE157204), and the rat CA1 soma–neuropil dataset

of Tushev et al. [11,26,27]. The Middleton and Perez analyses were performed at gene level using one annotation-prioritized representative 3′UTR per protein-coding gene, whereas the Tushev analysis used experimentally defined polyadenylation-site-supported (PASS) 3′UTR isoforms; the three resources therefore span two species, gene- and isoform-level representations, and distinct experimental definitions of subcellular localization. For Middleton, 3′UTR counts from the 16 cells with paired dendritic and somatic measurements were converted to counts per million per library, and a gene entered the dendritic candidate pool when it was detected in at least five dendritic samples, exceeded its somatic abundance in at least 10 of 16 paired cells, had a positive median paired log-fold difference and reached a mean dendritic abundance of 0.1 CPM; soma-enriched candidates used the reversed criteria, and candidates were ranked by concordant cell pairs, median paired log-fold difference and compartment-specific expression. For Perez, the authors' Dendrites and Somata classifications were used, and genes with an adjusted p below 0.05 and a concordant fold-change direction were retained, excluding ERCC controls, mitochondrial transcripts and genes without an eligible protein-coding 3′UTR. For Tushev, PASS records annotated as 3pUTR or 3pUTR_extended were retained and assigned to the neuropil- or somata-localized class, kept the isoform with the strongest absolute localization fold change per gene and group, and reserved genes represented in both groups for a separate within-gene analysis. For each resource, 250 localized and 250 somatic transcripts were selected jointly by matching log-transformed, standardized expression and 3′UTR length: mixed-integer optimization selected panels with balanced group means, one-to-one pairs were then assigned by minimizing Euclidean distance in the standardized matching space, and balance required an absolute standardized mean difference below 0.1 for both variables. Classification, sequence assignment and matching were completed before any nucleotide-composition or predicted rG4 feature was calculated, so the panels were frozen and sequence-blind.

3′UTR sequence assignment

For the gene-level datasets, transcript annotations and sequences were obtained from Ensembl release 116 using the GRCm39 mouse and GRCr8 rat assemblies [55]. Protein-coding genes and transcripts with an eligible 3'UTR were retained of at least 100 nucleotides and selected representative transcripts using annotation evidence in the order Ensembl canonical, MANE Select, APPRIS principal, CCDS support, transcript-support level, annotation level and transcript length. The 3′UTR was extracted as the cDNA sequence downstream of the uniquely matched coding sequence, and transcripts with missing or non-unique coding-sequence matches, empty 3′UTRs or 3′UTRs shorter than 100 nucleotides were excluded. For the Tushev isoform-level dataset, the PASS table specifies the distance between each polyadenylation site and its upstream stop codon but not complete genomic intervals, so each PASS-defined 3′UTR was reconstructed from the rn5 genome assembly and its RefGene annotation [56]. Strand was inferred from the PASS identifier and the published upstream length was projected from a strand-matched RefGene stop boundary; a sequence was retained only when the corresponding gene and strand had a unique stop boundary and the reconstructed length matched the reported upstream length. Isoforms with ambiguous stop boundaries, invalid intervals or reconstructed lengths outside 100–5,000 nucleotides were excluded rather than assigned heuristically.

Sequence-derived transcript coordinates

For each transcript or isoform in each frozen 500-member panel, we calculated the guanine fraction of the assigned 3′UTR and the predicted density of RNA G-quadruplex-forming regions. A candidate rG4 region was defined as four G-rich tracts of at least three consecutive guanines separated by loops of one to seven nucleotides, overlapping motif spans were merged, and the number of predicted regions was normalized per kilobase. This motif-based definition follows established computational G-quadruplex prediction and represents predicted rG4-forming-region density rather than experimentally measured G-quadruplex formation [57,58]. G fraction and predicted rG4 density were standardized separately within each frozen panel, and the primary sequence-derived coordinate was their mean (***Fig. 6A; Supplementary Note 5***). Additionally, G fraction alone was evaluated, predicted rG4 density alone, GC fraction, 3′UTR length, a relaxed motif definition using tracts of at least two guanines and loops of up to 12 nucleotides, and rG4 density residualized on standardized G fraction

and log 3′UTR length. Shuffled-score controls permuted the primary coordinate among transcript identities and random-score controls assigned independent normally distributed values; these alternatives were treated as decomposition, specificity and negative controls rather than equivalent measurements of RNP material properties.

PSD calibration and MSC integration

Published measurements of Shank3-dependent PSD condensate properties in wild-type and oligomerization-deficient conditions were used to anchor the postsynaptic side of the sequence-informed model [25]. Apparent elastic modulus, network relaxation time and Shank3 mobile fraction were each mapped independently onto a dimensionless PSD coordinate oriented from an ME-like state toward the stiffer, less mobile and more slowly relaxing WT-like state. For each observable, an oriented log-fold separation was normalized by the mean oriented separation across the three observables and scaled by a phenomenological cross-scale gain, and the resulting values defined symmetric WT-like and ME-like anchors. The three observables were mapped separately rather than combined, so that agreement among their predicted directions tests whether the result depends on a particular PSD measurement; because their coordinate separations differ by construction, their effect magnitudes are not quantitatively comparable, and the gain is phenomenological rather than a measured conversion between physical units and MSC material space. For the sequence-informed simulations, the transcript coordinate was inserted into the first dimension of the granule material vector and the corresponding PSD anchor defined the target position along that dimension, while the remaining coordinates were generated by the unchanged full-MSC material-pool procedure; this wrapper altered the transcript-associated material representation without changing the docking hazard, productive-capture rule, synaptic-state dynamics or hazard-to-probability conversion. Authentic and model-used transcript coordinates were stored separately, and the shuffled-mapping condition permuted coordinate assignments among sampled granules while preserving both the marginal distribution and the authentic transcript-associated values. WT-like and ME-like states were evaluated using matched parameter-generating seeds, with 100 seeds for network relaxation time and 30 seeds each for elastic modulus and mobile fraction, and event counts were normalized by the corresponding granule supply. Relative localized-cargo preference was calculated separately for active-synapse physical docking and productive capture as the supply-normalized localized event rate

divided by the sum of the localized and somatic rates, so that 0.5 indicates equal rates, and the log localized-to-somatic rate ratio was retained as an unbounded sensitivity metric. Sensitivity to the cross-scale mapping was evaluated for the relaxation-time mapping by multiplying the reference WT–ME separation by factors from zero to twice its reference value, using 30 matched seeds per condition for authentic and shuffled mappings.

Statistical analysis

Sequence-level differences were analysed using the one-to-one matched transcript or isoform pairs, with the mean within-pair localized-minus-somatic difference as the primary effect. Uncertainty was estimated from 20,000 bootstrap resamples of the matched pairs, two-sided empirical p-values from 20,000 random sign permutations of the paired differences, and multiple comparisons across the prespecified sequence scores were controlled by the Benjamini–Hochberg procedure and reported as q values [54]. Mann–Whitney tests and Cliff's delta were retained as complementary unpaired summaries. For the sequence-informed simulations, WT-like and ME-like outcomes were paired by parameter-generating seed, and state-specific preferences, WT-like minus ME-like shifts and authentic-minus-shuffled contrasts were summarized across seeds with 95% confidence intervals from seed-level bootstrap resampling and Benjamini–Hochberg correction across the prespecified coordinates, outcomes and PSD mappings. The sequence-informed analysis tests whether the MSC mechanism responds consistently to experimentally motivated transcript and PSD coordinates; it does not establish that the sequence coordinate measures RNP material identity, that G-rich sequence affects capture through condensate material properties in vivo, or that the PSD anchors reproduce biological material distances.

Data Availability

The transcriptomic datasets analysed in this study are publicly available. The mouse soma–dendrite dataset of Middleton et al. and the rat soma–dendrite dataset of Perez et al. are available from the Gene Expression Omnibus under accessions GSE115480 and GSE157204, respectively; the rat CA1 soma–neuropil PASS-level 3′UTR isoform data of Tushev et al. are available as supplementary resources of the original publication. Gene-level 3′UTR sequences were obtained from Ensembl release 116 (GRCm39, GRCr8), and PASS-defined isoform sequences were reconstructed from the rn5 assembly and its RefGene annotation available from the UCSC Genome Browser. Published PSD material measurements used for calibration were taken from Jia et al. The frozen transcript panels, matching diagnostics, processed plotting tables and all simulation outputs underlying ***Figs. 1–6*** and ***Figs. S1–5*** are available in the GitHub repository (https://github.com/ayberkalpgyunesh/Material-Selective-Capture-MSC)

Code Availability

All code required to reproduce the simulations, analyses and figures is openly available in the GitHub repository (https://github.com/ayberkalpgyunesh/Material-Selective-Capture-MSC) under the MIT licence. The repository contains the MSC simulator module (msc_model_feedback.py), the YAML configuration file specifying all 27 sampling intervals and fixed settings, the dynamic-material wrapper module, one self-contained notebook per figure, deterministic seed definitions, JSON run manifests with SHA-256 checksums of simulator and configuration files, and the R scripts used for the event-level logistic models, Holm-adjusted equivalence tests and odds ratios underlying ***Fig. 5***.
Simulations were implemented in Python 3; analyses and figures used NumPy [59], SciPy [60], pandas [61] , statsmodels [61,62] and Matplotlib [63], 3′UTR sequences were extracted from faidx-indexed FASTA files with pyfaidx [63,64] , and panel construction used the mixed-integer linear programming and linear-sum-assignment routines of SciPy [60]. Rerunning the notebooks with the archived base seeds reproduces all reported values, including the canonical 2,000,000 encounter observations and 6,079 docking events underlying ***Fig. 2***.

Acknowledgments

I am grateful to Barbara Arbeithuber for her valuable guidance on the direction of this work, helpful discussions, and review of the manuscript. The author received no specific funding for this work.

Author contributions

A.A.G. conceived the study, derived the analytical results, designed and implemented the computational model, performed all simulations and transcriptomic analyses, prepared the figures and wrote the manuscript.

Competing interests

The author declares no competing interests.

References

1. Sutton, M. A. & Schuman, E. M. Dendritic protein synthesis, synaptic plasticity, and memory. *Cell* **127**, 49–58 (2006).
2. Cohen, L. D. *et al.* Metabolic turnover of synaptic proteins: kinetics, interdependencies and implications for synaptic maintenance. *PLoS One* **8**, e63191 (2013).
3. Holt, C. E. & Schuman, E. M. The central dogma decentralized: new perspectives on RNA function and local translation in neurons. *Neuron* **80**, 648–657 (2013).
4. Redondo, R. L. & Morris, R. G. M. Making memories last: the synaptic tagging and capture hypothesis. *Nature Reviews Neuroscience* **12**, 17–30 (2010).
5. Sun, C. *et al.* The prevalence and specificity of local protein synthesis during neuronal synaptic plasticity. *Sci Adv* **7**, eabj0790 (2021).
6. Frey, U. & Morris, R. G. M. Synaptic tagging and long-term potentiation. *Nature* **385**, 533–536 (1997).
7. Das, S., Singer, R. H. & Yoon, Y. J. The travels of mRNAs in neurons: do they know where they are going? *Curr Opin Neurobiol* **57**, 110–116 (2019).
8. Doyle, M. & Kiebler, M. A. Mechanisms of dendritic mRNA transport and its role in synaptic tagging. *EMBO J* **30**, 3540–3552 (2011).
9. Bauer, K. E. *et al.* Live cell imaging reveals 3′-UTR dependent mRNA sorting to synapses. *Nature Communications* **10**, 3178 (2019).
10. Yoon, Y. J. *et al.* Glutamate-induced RNA localization and translation in neurons. *Proceedings of the National Academy of Sciences* **113**, E6877–E6886 (2016).
11. Tushev, G. *et al.* Alternative 3’ UTRs Modify the Localization, Regulatory Potential, Stability, and Plasticity of mRNAs in Neuronal Compartments. *Neuron* **98**, 495–511.e6 (2018).
12. Mayr, C. What Are 3’ UTRs Doing? *Cold Spring Harb Perspect Biol* **11**, (2019).

13. Song, M. S., Moon, H. C., Jeon, J.-H. & Park, H. Y. Neuronal messenger ribonucleoprotein transport follows an aging Lévy walk. *Nat Commun* **9**, 344 (2018).

14. Donlin-Asp, P. G., Polisseni, C., Klimek, R., Heckel, A. & Schuman, E. M. Differential regulation of local mRNA dynamics and translation following long-term potentiation and depression. *Proc Natl Acad Sci U S A* **118**, (2021).

15. Majumder, P. *et al.* Molecular switch of the dendrite-to-spine transport of TDP-43/FMRP-bound neuronal mRNAs and its impairment in ASD. *Cell Mol Biol Lett* **30**, 6 (2025).

16. Williams, A. H., O'Donnell, C., Sejnowski, T. J. & O'Leary, T. Dendritic trafficking faces physiologically critical speed-precision tradeoffs. *Elife* **5**, (2016).

17. Solouki, S., Mehrabi, F. & Mirzaii-Dizgah, I. Localization of long-term synaptic plasticity defects in cerebellar circuits using optokinetic reflex learning profile. *J Neural Eng* **19**, (2022).

18. Clopath, C., Ziegler, L., Vasilaki, E., Büsing, L. & Gerstner, W. Tag-trigger-consolidation: a model of early and late long-term-potentiation and depression. *PLoS Comput Biol* **4**, e1000248 (2008).

19. Bose, M., Rankovic, B., Mahamid, J. & Ephrussi, A. An architectural role of specific RNA-RNA interactions in oskar granules. *Nat Cell Biol* **26**, 1934–1942 (2024).

20. Langdon, E. M. *et al.* mRNA structure determines specificity of a polyQ-driven phase separation. *Science* **360**, 922–927 (2018).

21. Linsenmeier, M. *et al.* Dynamic arrest and aging of biomolecular condensates are modulated by low-complexity domains, RNA and biochemical activity. *Nat Commun* **13**, 3030 (2022).

22. Vidal Ceballos, A., Geissmann, A., Favaro, D. C., Deshpande, P. & Elbaum-Garfinkle, S. RNA guanine content and G-quadruplex structure tune the phase behavior and material properties of biomolecular condensates. *Sci Rep* **15**, 9295 (2025).

23. Zeng, M. *et al.* Phase Transition in Postsynaptic Densities Underlies Formation of Synaptic Complexes and Synaptic Plasticity. *Cell* **166**, 1163–1175.e12 (2016).

24. Zeng, M. *et al.* Reconstituted Postsynaptic Density as a Molecular Platform for Understanding Synapse Formation and Plasticity. *Cell* **174**, 1172–1187.e16 (2018).

25. Jia, B. *et al.* Shank3 oligomerization governs material properties of the postsynaptic density condensate and synaptic plasticity. *Cell* **188**, 6473–6491.e21 (2025).

26. Middleton, S. A., Eberwine, J. & Kim, J. Comprehensive catalog of dendritically localized mRNA isoforms from sub-cellular sequencing of single mouse neurons. *BMC Biol* **17**, 5 (2019).

27. Perez, J. D. *et al.* Subcellular sequencing of single neurons reveals the dendritic transcriptome of GABAergic interneurons. *Elife* **10**, (2021).

28. Fagre, C. & Gilbert, W. Beyond reader proteins: RNA binding proteins and RNA modifications in conversation to regulate gene expression. *Wiley Interdisciplinary Reviews: RNA* **15**, e1834 (2024).

29. Miura, P., Sanfilippo, P., Shenker, S. & Lai, E. C. Alternative polyadenylation in the nervous system: to what lengths will 3' UTR extensions take us? *Bioessays* **36**, 766–777 (2014).

30. Bae, B. & Miura, P. Emerging Roles for 3' UTRs in Neurons. *Int J Mol Sci* **21**, (2020).

31. An, J. J. *et al.* Distinct role of long 3' UTR BDNF mRNA in spine morphology and synaptic plasticity in hippocampal neurons. *Cell* **134**, 175–187 (2008).

32. Suhl, J. A. *et al.* A 3' untranslated region variant in FMR1 eliminates neuronal activity-dependent translation of FMRP by disrupting binding of the RNA-binding protein HuR. *Proc Natl Acad Sci U S A* **112**, E6553–61 (2015).

33. Miller, S. *et al.* Disruption of dendritic translation of CaMKIIalpha impairs stabilization of synaptic plasticity and memory consolidation. *Neuron* **36**, 507–519 (2002).

34. Höfler, S. & Duss, O. Interconnections between m6A RNA modification, RNA structure, and protein–RNA complex assembly. *Life Science Alliance* **7**, (2024).

35. Clavet-Fournier, V. *et al.* Pre- and postsynaptic nanostructures increase in size and complexity after induction of long-term potentiation. *iScience* **27**, 108679 (2024).

36. Yavas, A., van Putten, M., Ariyurek, Y. & Aartsma-Rus, A. Antisense oligonucleotide-mediated redirection of Igf1 alternative polyadenylation. *Neuromuscul Disord* **51**, 105394 (2025).

37. Vorlová, S. *et al.* Induction of antagonistic soluble decoy receptor tyrosine kinases by intronic polyA activation. *Mol Cell* **43**, 927–939 (2011).

38. Mei, Y. *et al.* Adult restoration of Shank3 expression rescues selective autistic-like phenotypes. *Nature* **530**, 481–484 (2016).

39. Gouveia, B. *et al.* Capillary forces generated by biomolecular condensates. *Nature* **609**, 255–264 (2022).

40. Feric, M. *et al.* Coexisting Liquid Phases Underlie Nucleolar Subcompartments. *Cell* **165**, 1686–1697 (2016).

41. Galvanetto, N. *et al.* Extreme dynamics in a biomolecular condensate. *Nature* **619**, 876–883 (2023).

42. Dörner, K. *et al.* Fluorescent protein and peptide tags alter condensate formation and dynamics in vivo and in vitro. *EMBO Rep* **27**, 89–121 (2026).

43. Fatti, E., Khawaja, S. & Weis, K. The dark side of fluorescent protein tagging-the impact of protein tags on biomolecular condensation. *Mol Biol Cell* **36**, br10 (2025).

44. Fonkeu, Y. *et al.* How mRNA Localization and Protein Synthesis Sites Influence Dendritic Protein Distribution and Dynamics. *Neuron* **103**, 1109–1122.e7 (2019).

45. Jawerth, L. *et al.* Protein condensates as aging Maxwell fluids. *Science* **370**, 1317–1323 (2020).

46. Alshareedah, I., Moosa, M. M., Pham, M., Potoyan, D. A. & Banerjee, P. R. Programmable viscoelasticity in protein-RNA condensates with disordered sticker-spacer polypeptides. *Nat Commun* **12**, 6620 (2021).

47. Chen, X. *et al.* Mass of the postsynaptic density and enumeration of three key molecules. *Proc Natl Acad Sci U S A* **102**, 11551–11556 (2005).

48. Chen, X. *et al.* Organization of the core structure of the postsynaptic density. *Proc Natl Acad Sci U S A* **105**, 4453–4458 (2008).

49. Smolen, P., Baxter, D. A. & Byrne, J. H. Molecular constraints on synaptic tagging and maintenance of long-term potentiation: a predictive model. *PLoS Comput Biol* **8**, e1002620 (2012).

50. Köhrmann, M. *et al.* Microtubule-dependent recruitment of Staufen-green fluorescent protein into large RNA-containing granules and subsequent dendritic transport in living hippocampal neurons. *Mol Biol Cell* **10**, 2945–2953 (1999).

51. Marino, S., Hogue, I. B., Ray, C. J. & Kirschner, D. E. A methodology for performing global uncertainty and sensitivity analysis in systems biology. *J Theor Biol* **254**, 178–196 (2008).

52. Lakens, D. Equivalence Tests: A Practical Primer for Tests, Correlations, and Meta-Analyses. *Soc Psychol Personal Sci* **8**, 355–362 (2017).

53. Aickin, M. & Gensler, H. Adjusting for multiple testing when reporting research results: the Bonferroni vs Holm methods. *Am J Public Health* **86**, 726–728 (1996).

54. Storey, J. D. & Tibshirani, R. Statistical significance for genomewide studies. *Proceedings of the National Academy of Sciences* **100**, 9440–9445 (2003).

55. Dyer, S. C. *et al.* Ensembl 2025. *Nucleic Acids Res* **53**, D948–D957 (2025).

56. Casper, J. *et al.* The UCSC Genome Browser database: 2026 update. *Nucleic Acids Res* **54**, D1331–D1335 (2026).

57. Bedrat, A., Lacroix, L. & Mergny, J.-L. Re-evaluation of G-quadruplex propensity with G4Hunter. *Nucleic Acids Res* **44**, 1746–1759 (2016).

58. Lombardi, E. P. & Londoño-Vallejo, A. A guide to computational methods for G-quadruplex prediction. *Nucleic Acids Res* **48**, 1603 (2020).

59. Harris, C. R. *et al.* Array programming with NumPy. *Nature* **585**, 357–362 (2020).

60. Virtanen, P. *et al.* Author Correction: SciPy 1.0: fundamental algorithms for scientific computing in Python. *Nat Methods* **17**, 352 (2020).

61. McKinney, W. Data Structures for Statistical Computing in Python. *SciPy 2010* https://doi.org/10.25080/Majora-92bf1922-00a (2010) doi:10.25080/Majora-92bf1922-00a.

62. Seabold, S. & Perktold, J. Statsmodels: Econometric and Statistical Modeling with Python. *SciPy 2010* https://doi.org/10.25080/Majora-92bf1922-011 (2010) doi:10.25080/Majora-92bf1922-011.

63. Hunter, J. D. Matplotlib: A 2D Graphics Environment. *Comput. Sci. Eng.* **9**, 90–95 (2007).

64. Website. https://doi.org/10.7287/peerj.preprints.970v1 doi:10.7287/peerj.preprints.970v1.

Supplementary Files

This is a list of supplementary files associated with this preprint. Click to download.

- GyuneshMSCSupplementaryInformation.docx